

The axis ratio distribution of X-ray clusters observed by XMM-Newton

Hajime Kawahara

Department of Physics, The University of Tokyo, Tokyo 113-0033, Japan

ABSTRACT

We derive the axis ratio distribution of X-ray clusters using the XMM-Newton catalogue (Snowden et al. 2008). By fitting the contour lines of the X-ray image by ellipses, we confirm the X-ray distribution is well approximated by the elliptic distribution with a constant axis ratio and direction. We construct a simple model describing the axis ratio of the X-ray gas assuming the hydrostatic equilibrium embedded in the triaxial dark matter halo model proposed by Jing & Suto (2002) and the hydrostatic equilibrium. We find that the observed axis ratio distribution is consistent with this model prediction. This is the first observational evidence in favor of the underlying triaxial dark halo model.

Subject headings: X-rays: galaxies: clusters, cosmology: observations, galaxies: clusters: general

1. Introduction

Galaxy clusters have been playing an important role in the determination of cosmological parameters such as the matter density, the amplitude of the initial fluctuation, the Hubble constant. Upcoming surveys of galaxy clusters via optical, X-ray, lensing and the Sunyaev-Zel'dovich effect will enable one to probe new aspects of cosmology such as the nature of the dark energy (e.g. Albrecht et al. 2006) and the initial non-Gaussianity. Therefore, the physical modeling of galaxy clusters is important to properly interpret the cluster data. In particular, non-sphericity adds significant uncertainty to various cosmological applications of the clusters (e.g. Oguri et al. 2003; Dalal et al. 2004).

The statistical nature of the non-sphericity has been investigated using N-body simulations by many authors (e.g. Jing & Suto 2002; Kasun & Evrard 2005; Paz et al. 2006; Bett et al. 2007). Among them, Jing & Suto (2002, hereafter JS02) proposed a triaxial model of the dark matter halo based on the detailed analysis of N-body simulations. They also provided the fitting formula of the probability distribution of the axis ratio.

Their phenomenological model has been applied to many studies that investigate the systematic errors of the cosmological applications with clusters. The observational test for the axis ratio distribution, however, is quite limited. Evans & Bridle (2009) analyzed 4281 clusters in the Sloan Digital Sky Survey using the gravitational lensing. By stacking all the clusters, they were merely able to conclude that the axis ratio of the projected dark matter halo $f = 0.48^{+0.14}_{-0.09}$. Due to large uncertainty, however, the measurement of the distribution of the axis ratio was difficult.

On the other hand, X-ray clusters also represent the non-sphericity, which makes the large statistical error to measurement of the Hubble constant (e.g Kawahara et al. 2008). There are several papers which measured the axis ratio of the X-ray clusters observed by Einstein (Buote & Canizares 1992; Mohr et al. 1995) and ROSAT (Buote & Canizares 1996; Wang & Ulmer 1997). The theoretical predictions of the axis ratio of X-ray clusters have been considered by several authors (e.g. Wang & Fan 2004; Lee & Suto 2004; Flores et al. 2007). These are based on the assumption that the non-sphericity of X-ray clusters originated from the non-spherical gravitational potential due to the dark matter halo. Therefore it is crucial to see if the non-sphericity of X-ray clusters can be explained by the non-sphericity of the underlying dark matter halo.

Nevertheless, no detail comparison the theoretical expectation with observation has been performed. The purpose of this paper is to examine the origin of the non-sphericity by comparing the detailed analysis of real clusters with the theoretical model.

The rest of the paper is organized as follows. In §2, we describe the cluster data we use and the data processing such as fitting clusters and estimating the statistical errors. In §3, in order to model the non-sphericity, we investigate the radial dependence of the axis ratio and the axis direction. After describing a simple model of the gas non-sphericity, we compare the non-spherical properties of X-ray clusters with the theoretical prediction. Finally, we summarize our results in §4.

2. Methods

We analyze 70 clusters in the XMM-Newton cluster catalogue (Snowden et al. 2008). The surface brightness map of each cluster is normalized by the exposure map and has the energy range of 0.5-10.0 keV band. Although XMM-Newton has three CCD imagers, 2 MOSs and pn, we simply combine the images of MOS1 and MOS2 and do not use the data of pn. Based on the light curve with the energy range of 10-15 keV, we exclude the period of " *flares* " due to the soft proton background from our analysis. The point sources

are also excluded by the wavelet detector in the CIAO package. The images are binned in a pixel size of 1 % of the virial radius r_{200} . The virial radius and mass are estimated by the relations found in the simulation, $r_{200} = 1.25 \times (1+z)^{-3/2} (T/10.0 \text{ keV})^{1/2} h^{-1} \text{ Mpc}$ and $M_{200} = 1.5 (T/10.0 \text{ keV})^{3/2} h^{-1} 10^{15} M_{\odot}$ (Evrard et al. 1996; Arnaud & Evrard 1999). We adopt the averaged cluster temperature in the $1' - 4'$ annulus given by Snowden et al. (2008).

We compute the circular average of the surface brightness, $\overline{S_X}(R)$ around the center identified as the brightest pixel. We fix the threshold of the contours $c_i = \overline{S_X}(R_i)$ where we adopt $R_i/r_{200} = 0.1, 0.2, 0.3$ and 0.4 for $i = 1, 2, 3$, and 4 . We draw the isocontour lines of c_i and fit them by ellipses if

$$N(R_i) - N_B(R_i) > 2\sqrt{N_B(R_i)}, \quad (1)$$

where $N(R_i)$ is the circular average of the photon counts per pixel, which is not normalized by the exposure map and $N_B(R_i) \equiv N(R_i)\overline{S_{X,B}}/c_i$ is the expected number of the background photons. The background level of the surface brightness $\overline{S_{X,B}}$ is adopted by the minimum level of $\overline{S_X}(R)$.

Figure 1 displays an example of the elliptical fitting. We exclude parts of contour lines in the masked region from the fitting. There are 62, 52, 27, and 5 clusters that satisfy equation (1) for $R/r_{200} = 0.1, 0.2, 0.3$ and 0.4 . We exclude 8 clusters, Coma, Perseus, A1060, M87, AWM7, A2256, A3888, and A3526 from our analysis because we cannot fit even $R/r_{200} = 0.1$ due to their redshifts or the virial radius or their position in the field of view. The elliptical fitting has three free parameters for the χ^2 statistics, the minor to major axis ratio, q , the direction of the long axis Θ , and the size of ellipse. We first perform the χ^2 fitting fixing the center position. After that, we adopt the minimum χ^2 as a function of the center position as the ellipse center. The statistical errors of q and Θ due to the Poisson noise are estimated by the Monte Carlo method. We create 100 mock clusters by redistributing the photon number according to Poisson distribution. The 1σ errors are derived by fitting the contour lines of each mock sample with the same fitting method. The average of errors for the axis ratio is $\overline{\sigma_q} = 0.035$.

3. Probability Distribution of the Axis Ratio

Figure 2 shows the radial dependence of the projected axis ratio and the axis direction. In the upper panel, we plot the average of q for clusters as a function of R/r_{200} . Although there is a slight increment of the axis ratio with z , the difference between $R/r_{200} = 0.1$ and 0.3 does not significantly change (≈ 0.04). The lower panel shows the radial dependence of the difference of $\Theta(R_i)$ around the radial average, $\Delta\Theta(R_i) \equiv \Theta(R_i) - \overline{\Theta}$. The average

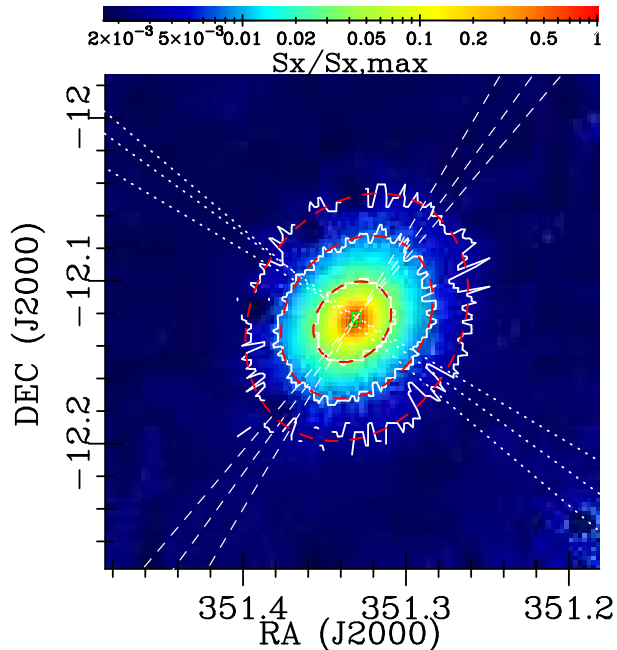


Fig. 1.— An example of the elliptical fitting of the X-ray cluster (A2597). Solid curves are the contour lines with $R/r_{200} = 0.1, 0.2,$ and 0.3 . Red dashed curves are the fitting ellipse. Three white dashed and dotted lines indicates the direction of the major and minor axes, respectively.

axis direction $\bar{\Theta}$ is computed from the average of the unit vector with an angle $\Theta(R_i)$, $\bar{\Theta} \equiv \arccos [u_x / (u_x^2 + u_y^2)^{1/2}]$, where $u_x = \sum_i \cos \Theta(R_i)$ and $u_y = \sum_i \sin \Theta(R_i)$. For most clusters, the axis directions are aligned within 10 degree. The points with $\Delta\Theta > \pi/8$ have large errors as displayed by color. These large statistical errors of the axis direction mainly originate from the uncertainty due to their high axis ratio (near spherical). Despite some variations of the axis ratio and the axis direction, we find that the surface brightness contours are well approximated by the ellipses with the same direction and axis ratio for different radii.

JS02 reported the negative redshift dependence and the (slightly) positive mass dependence on the axis ratio. Figure 3 displays the redshift and mass dependence of the axis ratio. Since the present XMM-newton catalogue is heterogeneous, Figure 3 does not show any clear dependence of the axis ratio on z or M_{200} .

Let us compare the observed axis ratio distribution of X-ray halo with a theoretical expectation. We first construct a simple model of the axis ratio distribution of the X-ray halo based on the triaxial model of the dark matter halo. Our assumptions are as follows, 1) The dark matter halo is a homeoid ellipsoid. (has the constant axis ratio and perfect

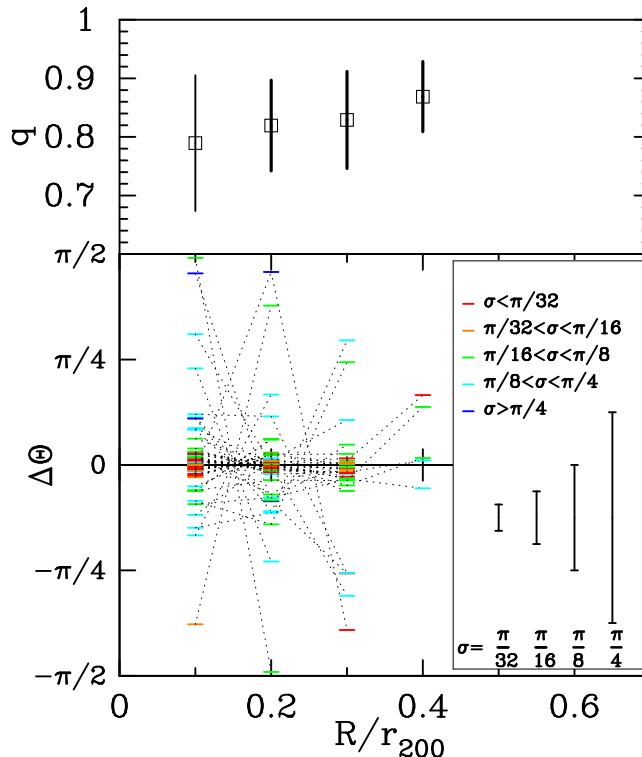


Fig. 2.— Radial dependences of the projected axis-ratio and the axis direction. The upper panel shows the average profile of the axis ratio q . We average over 62, 52, 27, and 5 clusters for $R/r_{200} = 0.1, 0.2, 0.3$ and 0.4 , respectively. Black errors indicate the standard deviation for clusters. The Lower panel display the difference of the axis direction, $\Delta\Theta(R_i) \equiv \Theta(R_i) - \bar{\Theta}$. The average axis direction $\bar{\Theta}$ is derived by the average of the unit vector with $\Theta(R_i)$, $\bar{\Theta} = \arccos [u_x / (u_x^2 + u_y^2)^{1/2}]$, where $u_x = \sum_i \cos \Theta(R_i)$ and $u_y = \sum_i \sin \Theta(R_i)$. Each dashed line connects $\Delta\Theta$ for different radii of an identical cluster. Each color indicates the standard deviation of $\Theta(R_i)$ for the j -th cluster $\sigma_{\Theta,j}$: red, orange, green, cyan, and blue.

alignment of the axis direction). 2) The gas distribution is perfectly governed by the dark matter potential through the hydrostatic equilibrium. In other words, we neglect the self gravity of the gas and regard a cluster as a completely relaxed system. 3) The X-ray surface brightness distribution depends on the gas density only, that is, we assume that the cluster is isothermal. Although the actual simulated halo shows a slight radial dependence of the axis ratio as reported by JS02 (see Figure 3 of their paper), we assume the constant axis model.

JS02 suggested the triaxial density model with three axes $a_1 \geq a_2 \geq a_3$ described as

$$\rho(\tilde{R}) = \frac{\rho_0}{(\tilde{R}/\tilde{R}_s)^\alpha [1 + (\tilde{R}/\tilde{R}_s)^{3-\alpha}]}, \quad (2)$$

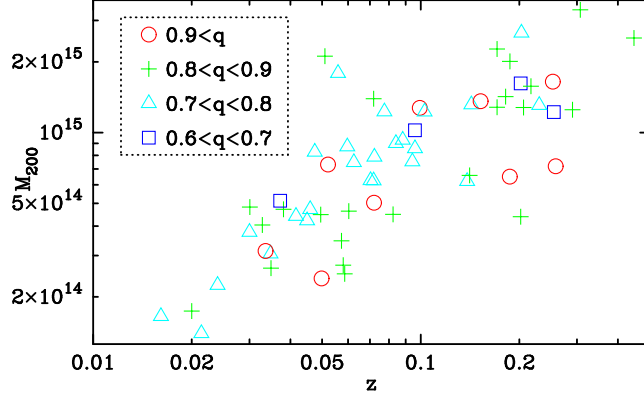


Fig. 3.— Scatter plot of clusters with different axis ratio on a z - M_{200} plane. Different types of symbols indicate the axis ratio of the cluster: $0.9 < q$ (circle), $0.8 < q < 0.9$ (cross), $0.7 < q < 0.8$ (triangle), and $0.6 < q < 0.7$ (square).

where $\alpha = 1$ for the cluster size halo (the triaxial NFW profile), $\alpha = 1.5$ for the galaxy size halo and \tilde{R} is the major axis length:

$$\tilde{R}^2 = x^2 + y^2/\mu_B^2 + z^2/\mu_A^2. \quad (3)$$

where $\mu_A \equiv a_3/a_1$ and $\mu_B \equiv a_2/a_1$ denote the minor-to-major and medium-to-major axis ratio, respectively. JS02 also provided the fitting formula of the joint probability density function (PDF) of μ_A and μ_B at $A^{(3)} = 2500$, $p_{\text{DM}}(\mu_A, \mu_B; M_{200}; z) = p_A(\mu_A; M_{200}; z)p_B(\mu_B|\mu_A)$, where

$$\begin{aligned} p_A(\mu_A; M_{200}; z) &= \frac{1}{\sqrt{2\pi}\sigma_s} \exp\left\{-\frac{[\mu_A g(M_{200}, z) - 0.54]^2}{2\sigma_s^2}\right\}, \\ p_B(\mu_B|\mu_A) &= \frac{3}{2(1-r_{\min})} \left[1 - \left(\frac{2\mu_B - 1 - r_{\min}}{1 - r_{\min}}\right)^2\right], \\ g(M_{200}, z) &\equiv \left(\frac{M_{200}}{M_*}\right)^{0.07\Omega(z)^{0.7}}, \end{aligned} \quad (4)$$

where M_* is the characteristic nonlinear mass at z so that the rms top-hat smoothed over density at the scale is 1.68, $\sigma_s = 0.113$, and $r_{\min} = \mu_A$ for $\mu_A \geq 0.5$ and $r_{\min} = 0.5$ for $\mu_A < 0.5$. The $A_{(3)}$ is \tilde{R} with which the ellipsoid having overdensity 2500. Note that $A_{(3)} = 2500$ corresponds to the typical radius $\approx 0.3 r_{200}$.

Under the hydrostatic equilibrium assumption, the gas isodensity surface is identical to the isopotential surface. The potential of a homeoid at the position (x, y, z) is provided by

Binney & Tremaine (1987),

$$\begin{aligned}\Phi(x, y, z) &= -\pi G \left(\frac{a_2 a_3}{a_1} \right) \int_0^\infty \frac{\psi(\infty) - \psi(m)}{\sqrt{(a_1^2 + \tau)(a_2^2 + \tau)(a_3^2 + \tau)}} d\tau \\ \psi(m) &= 2 \int_0^m \rho(\tilde{R}) \tilde{R} d\tilde{R} \\ m^2 &\equiv \frac{x^2}{\tau + 1} + \frac{y^2}{\tau + \mu_B^2} + \frac{z^2}{\tau + \mu_A^2}\end{aligned}\quad (5)$$

Assuming the density distribution in equation (2), we obtain

$$\psi(m) = \frac{2\tilde{R}_s^2 \rho_0}{2 - \alpha} \left(1 + \frac{\tilde{R}_s}{m} \right)^{\alpha - 2}.\quad (6)$$

We can rewritten the potential as,

$$\begin{aligned}\Phi(x', y', z') &= -2\pi G \frac{\tilde{R}_s^2 \rho_0}{\alpha - 2} \mu_A \mu_B \Xi(x', y', z') \\ \Xi(x', y', z') &\equiv \int_0^\infty \frac{1 - [1 + (m')^{-1}]^{\alpha - 2}}{\sqrt{(1 + \tau)(\mu_B^2 + \tau)(\mu_A^2 + \tau)}} d\tau,\end{aligned}\quad (7)$$

$$(8)$$

where x', y', z' and m' denote x, y, z and m normalized by \tilde{R}_s , respectively. Although Lee & Suto (2004) provided a perturbative approach to solve Φ , we directly derive the axis ratio by numerical integrations. The isopotential surface defined by $\Phi(x, y, z) = \text{const} = \Phi(x_*, 0, 0)$ can be approximated by the triaxial ellipsoid with the minor to major and the medium to major axis ratio,

$$\mu_{g,A}(\mu_A, \mu_B; x'_*) \equiv \frac{z'_*}{x'_*}, \text{ and}\quad (9)$$

$$\mu_{g,B}(\mu_A, \mu_B; x'_*) \equiv \frac{y'_*}{x'_*},\quad (10)$$

where y'_* and z'_* are obtained by solving following relations,

$$\Xi(x'_*, 0, 0) = \Xi(0, 0, z'_*) = \text{const},\quad (11)$$

$$\Xi(x'_*, 0, 0) = \Xi(0, y'_*, 0) = \text{const}.\quad (12)$$

Thus, we regard that the gas density distribution as an ellipsoid with constant axis ratios $\mu_{g,A}$ and $\mu_{g,B}$.

One uncertainty of this model is the choice of x'_* . Because the fitting formula given in equation (4) is based on $\tilde{R} \approx 0.3 r_{200}$, it is natural to adopt $x'_* = 0.3 r_{200} / \tilde{R}_s = 0.3 c$, where c is the concentration parameter. It is impossible to know c from X-ray observation only. We assume the typical value $c = 3$ found in simulations (JS02). Because most contour lines we investigate are below $0.3 r_{200}$, we also consider $x'_* = 0.3, 0.6$ which approximately corresponds to the contours $i = 1, 2$ in addition to 0.9 ($i = 3$).

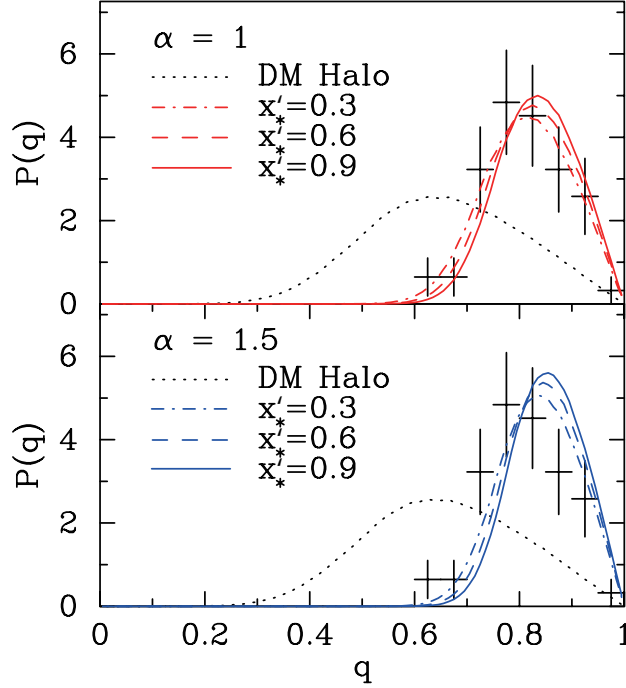


Fig. 4.— Comparison the theoretical prediction of the axis ratio distribution (lines) with observation (error bars). We use *the radial averaged* axis ratio of each cluster. Error bars are Poissonian. Lines in the top (bottom) panel are theoretical curves with the density profile (Eq.[2]) with $\alpha = 1$ ($\alpha = 1.5$). Solid, dashed, and dot-dashed lines indicate $x'_* = 0.9, 0.6$ and 0.3 , respectively. For reference, we plot the axis ratio distribution of the underlying dark matter halo, which is expected from the lensing observation for instance.

The axis ratio of the ellipse made by the projection of the ellipsoid is obtained by (Binney 1985)

$$\hat{q}(\theta, \phi; \mu_{g,A}, \mu_{g,B}) = \sqrt{\frac{A + C - \sqrt{(A - C)^2 + B^2}}{A + C + \sqrt{(A - C)^2 + B^2}}}$$

$$A \equiv \mu_{g,A}^{-2} \cos^2 \theta (\sin^2 \phi + \mu_{g,B}^{-2} \cos^2 \phi) + \mu_{g,B}^{-2} \sin^2 \theta$$

$$B \equiv \mu_{g,A}^{-2} (1 - \mu_{g,B}^{-2}) \cos \theta \sin 2\phi$$

$$C \equiv \mu_{g,A}^{-2}(\mu_{g,B}^{-2} \sin^2 \phi + \cos^2 \phi), \quad (13)$$

where θ and ϕ are the polar coordinates of the line of sight. The PDF of the projected axis ratio is given by

$$\begin{aligned} p(q; x'_*; M_{200}; z) &= \frac{1}{4\pi} \int_0^{2\pi} d\phi \int_0^\pi \sin \theta d\theta \int_{\mu_B}^1 d\mu_A \int_0^1 d\mu_B \\ &\times \delta_D(q - \hat{q}(\theta, \phi; \mu_{g,A}(\mu_A, \mu_B; x'_*), \mu_{g,A}(\mu_A, \mu_B; x'_*))) \\ &\times p_{\text{DM}}(\mu_A, \mu_B; M_{200}; z), \end{aligned} \quad (14)$$

where $\delta_D(x)$ is the delta function. The PDF averaged by the virial mass and the redshift of the cluster sample is given by

$$P(q; x'_*) \equiv \frac{1}{N} \sum_{i=1}^N p(q; x'_*; M_{200,i}; z_i). \quad (15)$$

Figure 4 displays the observed axis ratio distribution and the theoretical prediction described in equation 15. Because the radial dependence of the ellipse is relatively small, we adopt the radial average for each cluster as the observed axis ratio. We plot the theoretical prediction described in equation (15) by performing Monte Carlo methods. The number of realization for each cluster is 128^2 . The top and bottom panels show the results for $\alpha = 1.0$ and 1.5, respectively. We find that both models significantly agree with observational result although the NFW triaxial model is slightly better than that of $\alpha = 1.5$. We also confirm that the model uncertainty due to the selection of x'_* is relatively small.

4. Conclusion and Summary

In this paper, we have examined the axis ratio distribution of X-ray halos using the XMM-Newton cluster catalogue. By fitting the surface brightness contours by ellipses, we confirmed that the radial dependence of the axis ratio and the axis direction is relatively small, that is, the X-ray halo is well approximated by the triaxial ellipsoid. Constructing the simple model based on the hydrostatic equilibrium of the underlying triaxial dark matter halo proposed by Jing & Suto (2002), we found that the observed PDF of the axis ratio of X-ray halo agrees well with the theoretical prediction. The present result supports the triaxial model of the dark halo predicted in the context of the standard Λ CDM model.

We are deeply grateful to Akio Hoshino for his instruction of the X-ray analysis. We also thank Takahiro Nishimichi, Thierry Sousbie, and Yasushi Suto for useful discussions. HK

is supported by a JSPS (Japan Society for Promotion of Science) Grant-in-Aid for science fellows. This work is also supported by Grant-in-Aid for Scientific research from JSPS and from the Japanese Ministry of Education, Culture, Sports, Science and Technology (Nos. 20-10466), and by the JSPS Core-to-Core Program “International Research Network for Dark Energy”.

REFERENCES

- Albrecht, A., Bernstein, G., Cahn, R., Freedman, W. L., Hewitt, J., Hu, W., Huth, J., Kamionkowski, M., Kolb, E. W., Knox, L., Mather, J. C., Staggs, S., & Suntzeff, N. B. 2006, ArXiv Astrophysics e-prints
- Arnaud, M., & Evrard, A. E. 1999, MNRAS, 305, 631
- Bett, P., Eke, V., Frenk, C. S., Jenkins, A., Helly, J., & Navarro, J. 2007, MNRAS, 376, 215
- Binney, J. 1985, MNRAS, 212, 767
- Binney, J., & Tremaine, S. 1987, Galactic dynamics, ed. S. Binney, J. & Tremaine
- Buote, D. A., & Canizares, C. R. 1992, ApJ, 400, 385
- . 1996, ApJ, 457, 565
- Dalal, N., Holder, G., & Hennawi, J. F. 2004, ApJ, 609, 50
- Evans, A. K. D., & Bridle, S. 2009, ApJ, 695, 1446
- Evrard, A. E., Metzler, C. A., & Navarro, J. F. 1996, ApJ, 469, 494
- Flores, R. A., Allgood, B., Kravtsov, A. V., Primack, J. R., Buote, D. A., & Bullock, J. S. 2007, MNRAS, 377, 883
- Jing, Y. P., & Suto, Y. 2002, ApJ, 574, 538
- Kasun, S. F., & Evrard, A. E. 2005, ApJ, 629, 781
- Kawahara, H., Kitayama, T., Sasaki, S., & Suto, Y. 2008, ApJ, 674, 11
- Lee, J., & Suto, Y. 2004, ApJ, 601, 599
- Mohr, J. J., Evrard, A. E., Fabricant, D. G., & Geller, M. J. 1995, ApJ, 447, 8
- Oguri, M., Lee, J., & Suto, Y. 2003, ApJ, 599, 7

- Paz, D. J., Lambas, D. G., Padilla, N., & Merchán, M. 2006, *MNRAS*, 366, 1503
- Snowden, S. L., Mushotzky, R. F., Kuntz, K. D., & Davis, D. S. 2008, *A&A*, 478, 615
- Wang, Q. D., & Ulmer, M. P. 1997, *MNRAS*, 292, 920
- Wang, Y., & Fan, Z. 2004, *ApJ*, 617, 847